Laser-Assisted Field Evaporation of Chromia with Deep Ultraviolet Laser Light

Laser-Assisted Field Evaporation of Chromia with Deep Ultraviolet Laser Light

Severin Jakob, Andrea Fazi, Mattias Thuvander

Microscopy and Microanalysis, 2025, **31**, ozae111
https://doi.org/10.1093/mam/ozae111
Advance access publication 14 November 2024
Original Article

Microscopy AND Microanalysis

Laser-Assisted Field Evaporation of Chromia with Deep Ultraviolet Laser Light

Severin Jakob*, **Andrea Fazi**, **and Mattias Thuvander***

Department of Physics, Chalmers University of Technology, SE-412 96 Göteborg, Sweden

***Corresponding author:** Severin Jakob, E-mail: severin.jakob@chalmers.se; Mattias Thuvander, E-mail: mattias.thuvander@chalmers.se

Abstract

In this work, samples of chromia (Cr_2O_3) scale have been prepared for atom probe tomography and field evaporated with deep ultraviolet laser light (258 nm wavelength). The investigated range of laser energies spans more than three orders of magnitude between 0.03 and 90 pJ. Furthermore, the effects of detection rate and temperature were investigated. Simultaneous voltage and laser pulses were employed on additional needle specimens to reduce the standing voltage and minimize background noise during the measurement. Smooth evaporation with minimal mass spectrum peak tails was maintained over the whole range of measurement parameters. High laser energies result in significant underestimation of the oxygen content. Only laser energies below 1 pJ resulted in measured values near the expected oxygen content of 60 at%, the closest being about 58 at%.

Key words: atom probe tomography, chromia, laser-assisted atom probe tomography, oxide, oxygen quantification, parameter study

Introduction

Atom probe tomography (APT) provides information on the local chemistry of materials. A needle-shaped specimen is placed in a high electric field and exposed to a voltage pulse to initiate field evaporation. The generated ions are accelerated toward a position-sensitive detector and identified with time-of-flight mass spectrometry. The method offers atomic resolution with high sensitivity for all elements (Gault et al., 2012; Larson et al., 2013; Miller & Forbes, 2014). Originally, the analysis was limited to conducting materials, i.e., metals and alloys. However, the advent of laser-assisted APT made the measurement of nonconductive materials possible (Gault et al., 2006; Oberdorfer et al., 2007; Stiller et al., 2016; Devaraj et al., 2018). The use of laser light with wavelength in the ultraviolet (UV) spectrum shows usually better mass resolution and performance than green or infrared light (Hono et al., 2011; Lu et al., 2017). Accordingly, the commercial APT instruments switched through the generations from green (LEAP 3000, 532 nm wavelength) to UV (LEAP 4000 and LEAP 5000, 355 nm) to deep UV (LEAP 6000, 258 nm) laser light (Devaraj et al., 2018; Ulfig et al., 2022).

Investigations of compounds, such as oxides, carbides, nitrides, and borides, are challenging and often show an understoichiometric composition (Tang et al., 2010; Mancini et al., 2014; Morris et al., 2022, 2024). The loss of certain species can happen due to detector pile-up, where the impacts of more than one ion in close proximity in time and space cannot be resolved with the detector systems currently used (Thuvander et al., 2011, 2019; Meisenkothen et al., 2015; Peng et al., 2018). With oxide and nitride samples, APT measurements often lead to field evaporation of molecular ions (Saxey, 2011; Santhanagopalan et al., 2015; Blum et al., 2016). These ions can undergo dissociation processes that in part result in neutral molecules (Gault et al., 2016; Morris et al., 2022).

Thermally grown chromia (Cr_2O_3) is used as protective oxide in high-temperature applications (Nguyen et al., 2015; Young, 2016; Chyrkin et al., 2022). It is formed as a protective layer from Cr within the base alloy, e.g., during oxidation of stainless steel and Ni-based superalloys. The chromia scale incorporates elements from the base material, influencing the properties of the oxide (Chyrkin et al., 2011). In this paper, we report on the laser-assisted field evaporation of specimens from chromia scales with deep UV laser light in a LEAP 6000 XR. This tool is rather new, and hence, characterization of different materials utilizing laser light with not yet investigated photon energy is highly desired. Different measurement parameters, in particular, laser pulse energy (LPE) as well as detection rate (DR) and temperature, are investigated to identify a parameter window for optimal composition measurements.

Materials and Methods

Chromia scale was thermally grown on Ni-based alloy Inconel 625 at 900°C for 1000 h in laboratory air. The oxide thickness was 3–5 μm. Further details on the investigated material can be found elsewhere (Chyrkin et al., 2011, 2022). APT specimens were prepared via focused ion beam (FIB) lift-out in the dual-beam FEI Versa 3D workstation (Hillsboro, OR, USA) implementing well-known procedures for sample lift-out and preparation (Thompson et al., 2007; Langford & Rogers, 2008). Scanning electron micrographs of the cross-

Received: April 26, 2024. **Revised:** September 17, 2024. **Accepted:** October 23, 2024

section of the chromia scale and the microtip before APT measurement in laser mode are depicted in Supplementary Figure S1 in the supplementary material. APT measurements of chromia were performed in a LEAP 6000 XR from CAMECA (Madison, WI, USA). The instrument is equipped with a reflectron and has 52% detection efficiency. The LPE of the deep UV laser (258 nm wavelength) was varied between 0.03 and 90 pJ. Furthermore, measurements were performed with simultaneous voltage and laser (V + L) pulsing, with 20% voltage pulse and LPEs between 0.05 and 50 pJ. The measurements were primarily performed at 200 kHz and 40 K (data points of 90 and 70 pJ were measured at 170 kHz). The DR was varied between 0.2 and 2%, and the effect of temperature was investigated between 25 and 100 K. About one million ions were sampled for each parameter set (except for the lowest LPE due to fracture of the specimen), and the data were evaluated with the commercial software AP Suite 6.3 (CAMECA). The background values, expressed as ppm/ns, are taken from the initial step in the reconstruction wizard. For compositional measurements, the "local range-assisted' background reduction with a power law fit within AP Suite was used. The O composition was calculated with the following peak assignments for two peaks with possible overlaps: 16 Da O^+, 32 Da TiO^{++}. Peak assignment and deconvolution are discussed at the beginning of the Discussion section.

Results

After the initial turn-on of the specimen, evaporation was maintained until the run had stabilized without a remaining Ga signal coming from the FIB preparation. Subsequently, about one million ions were collected for each LPE. The standing voltage increased with every decreasing step in LPE (as a higher electrostatic field is needed to maintain a constant DR when using a lower LPE). The portion of ions for evaluation was chosen to avoid this initial voltage increase. Figure 1a shows the evolution of the standing voltage and the background signal as a function of ion sequence during the variation of LPE for laser pulse mode. This measurement was performed on the same specimen with 0.5% DR. As can be seen on the *x*-axis, the measurement ran for more than 100 million ions in between the LPE variation. The voltage increases only slightly during evaporation, which speaks for a small shank angle of the specimen. For lower LPEs, the background signal increases and hence impairs accurate quantification for low signal-to-noise peaks (Oltman et al., 2009; Haley et al., 2020). To reduce the standing voltage, and hence the background signal, simultaneous V + L pulsing was employed. The corresponding voltage and background evolution is depicted in Figure 1b. The noise is reduced by more than a factor of two. The background signal for all runs shows a close dependence with LPE as follows: Background = constant∗$LPE^{-0.5}$. The background as a function of LPE and the power law fits are depicted in Supplementary Figure S2 in the supplementary material.

Figure 2 shows mass spectra of sections with different LPE. The main contributions of ions are O^+, Cr^{++}, CrO^{++}, CrO_2^{++}, CrO^+, CrO_2^+, and CrO_3^+. Additionally, some Ti and its oxide ions can be found, leading to about 2–3 at% Ti in the chromia. Aluminum has a concentration of about 0.2–0.3 at%, and other elements combined amount to less than 0.2 at%. At high LPEs, molecular ions such as $Cr_2O_3^+$, $Cr_2O_3^{++}$, and $Cr_2O_4^+$ are measured, whereas these ions are missing at lower LPEs (i.e., higher field). Similarly, Cr^+ is apparent at high LPEs, but shows diminishing fractions with lower LPEs. Figure 2d shows the mass spectra of the sections of the laser run as well as a V + L run with a LPE of 0.1 pJ. The apparent ions are the same, and the V + L run shows less background noise compared to the laser run. The fractions of the most relevant ions as a function of LPE are depicted in Figure 3. At low LPEs, CrO^{++} is dominant. With increasing LPE, CrO^{++} and CrO_2^{++} are decreasing. In contrast, O^+ and Cr^{++} are increasing with higher LPE. At 2 pJ (laser run) and 2–5 pJ (V + L), the highest fraction of O^+ is reached. Applying higher LPE leads to a decrease in the fraction of O^+ as well as a continued decrease of CrO^{++} and an increase of Cr^{++}. Other ions seen in the mass spectra like Cr^+ and heavier molecular ions account for fractions below 5% and are only shown in Supplementary Figure S3 in the supplementary material and not in Figure 3 for visibility reasons. The errors of ion concentrations as well as atomic O concentrations are derived from number statistics (one sigma) in AP Suite, which is a minimal bound for variance since peak ranging, overlaps, etc., likely have larger influence but are rarely quantifiable (Danoix et al., 2007; London, 2019). The statistical errors are smaller than 0.1% for the lowest LPE with limited number of ions due to sample fracture. Errors for all other data points are below 0.05%, which is smaller than the symbol size, and hence, error bars are not shown in the diagrams for better visualization.

Figure 4a shows the measured O concentration as a function of LPE. The O content at 90 pJ is 37 at%, which is significantly lower than the expected stoichiometric concentration of 60 at%. With decreasing LPE, the O concentration is increasing. At LPE of <1 pJ a plateau value of about 58 at% is reached and maintained until the concentration falls marginally for LPEs below 0.04 pJ. The effect of different DRs was investigated during the second V + L run at 10 pJ LPE. The O concentration is increasing significantly with higher DR. The LPE variation with 1% DR gives higher O concentrations than the runs with 0.5% DR, confirming the improved accuracy with higher DR. Figure 4c shows the influence of temperature on the O concentration. A slight increase toward the expected O concentration is observed with increasing temperature. This effect is less pronounced than the influence of DR.

Discussion

The peak at 16 Da could stem from O^+ or O_2^{++}. This declaration influences the oxygen content drastically. Investigation of ^{18}O-enriched hematite (α-Fe_2O_3) showed that the 16 Da peak came predominately from O^+ (Bachhav et al., 2013) in that case. The peak was ranged as O^+ in this work as well, assuming that the evaporation of the two oxides is not significantly different. Another work with 1:1 ratio of ^{16}O and ^{18}O during oxidation of a Ni-based superalloy showed an overall contribution to the O concentration of about 1 at% from O_2^{++} ions (Viskari et al., 2013). It can be noted that the occurrence of X_2^{++} seems to be unusual also for B, C, and N. Similarly, the small peak at 32 Da could come from O_2^+ or TiO^{++}. The number of ions from the four Ti isotopes with low abundance indicates that the 32 Da peak is predominantly TiO^{++} and hence was ranged accordingly. The reported O concentrations correspond therefore to the lower bound of possible outcomes of each measurement of the O concentration. An exemplary deconvolution of peak overlaps with the APT

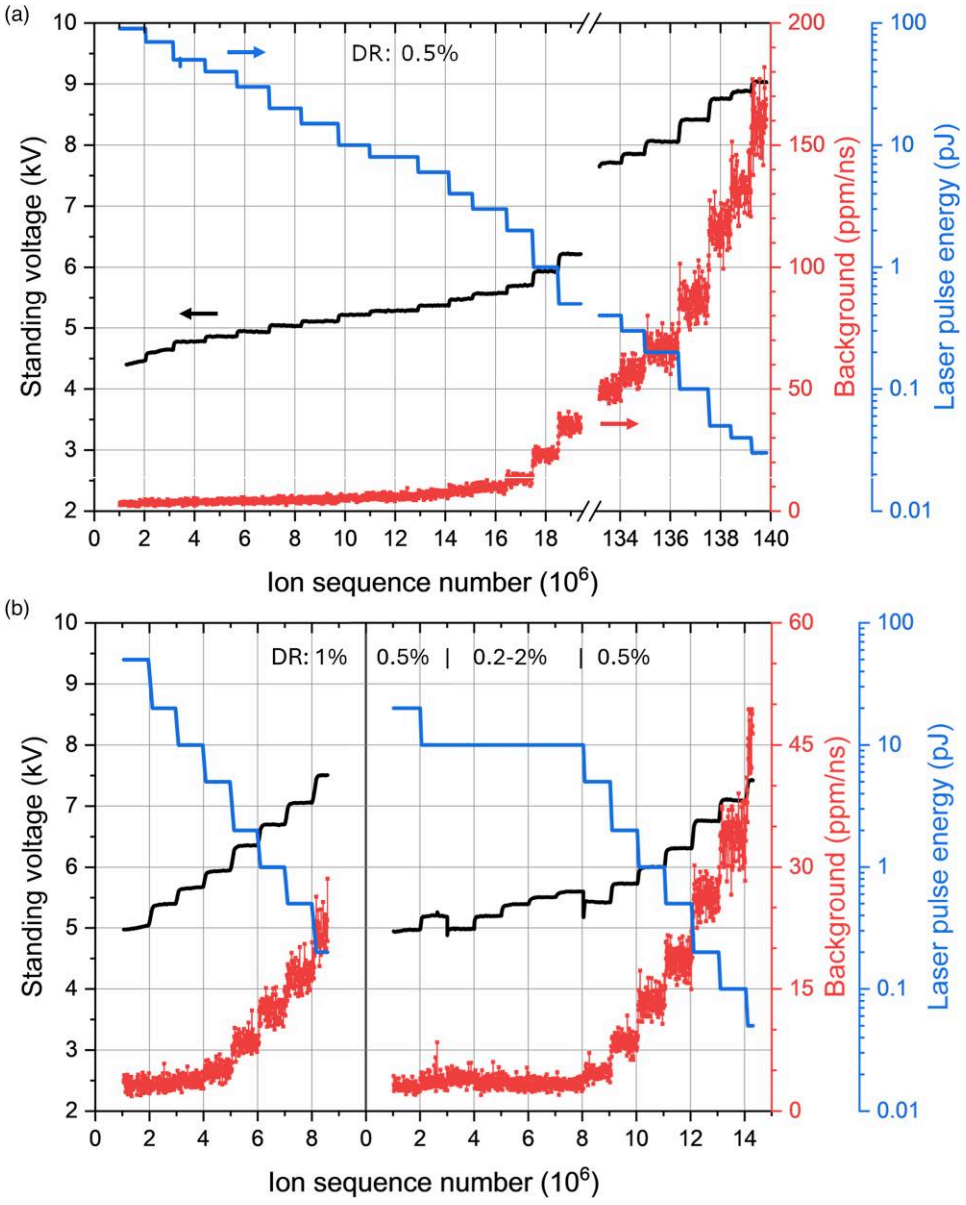

Fig. 1. (a) Voltage and background history as a function of ion sequence (detected ions) for the variation of LPE in the laser run. (b) Voltage and background history during measurements with simultaneous V + L pulsing. Note that the background scales are different.

software was performed for the section of the laser run at 1 pJ LPE. Table 1 presents the possible ions near 16 and 32 Da. The natural abundances as well as the deconvoluted counts are displayed. Initially, with the assignments described above and without using deconvolution of overlapping peaks, the O concentration was 56.0 at%. The peak deconvolution yields additional 26,496 O counts and an O concentration of 57.2 at%. Most of these counts come from the peak at 16 Da. However, the only peak solely declared as O_2^{++} at 16.5 Da shows no counts above the background. Thus, the deconvolution of the 16 Da peak has limited foundation and infers a large uncertainty. The deconvolution at 32 Da identifies a small fraction of O_2^{+} that raises the overall O concentration by 0.04 at %. Defining an upper bound for the O concentration is difficult since the accurate division between O_2^{++} and O^+ at 16 Da is not known. Ranging the peak at 16 Da as solely O_2^{+} leads to an overall O concentration of 63.7 at%, which is higher than the expected value. This peak assignment seems rather improbable due to the absence of a clear 16.5 Da peak.

So far, the expected stoichiometry was taken to be 60 at%, which is the case for pure Cr_2O_3. In addition to Cr and O, about 2–3 at% of other elements, mostly Ti, are present in the analyses of the oxide. Ti segregates to the grain boundaries as well as being incorporated into the matrix. For elements that are segregated, the ratio of O to Cr should be unaffected and amount to 1.5. The values for our material are presented in Supplementary Figure S4 in the supplementary material and approach this value to about 1.45, suggesting that some O is still missing. Chromia with incorporated Ti might be written as $Cr_{2-x}Ti_xO_3$, and thus, the expected stoichiometry is still 60 at% O.

The field at the apex of the needle-shaped specimen can be estimated by the charge state ratios (CSRs) according to Kingham (1982). The CSR of Cr^{++}/Cr^{+} was obtained for all

LPE; however, measurements at low LPEs incurred low Cr^+ counts and high background. Furthermore, dissociations might influence the CSR of metallic Cr significantly (Schreiber et al., 2014). Therefore, in order to estimate the field for different LPEs, the initial Cr^{++}/Cr^+ CSR during the laser run at 90 pJ LPE with the value of 32 was used to estimate the electrostatic field for this data point (using the Kingham curves) to be 23 V/nm. Subsequently, the fields for all further data points of the laser run were calculated using the increase in standing voltage relative to the voltage for the initial LPE. In this way, the relative electrostatic fields can be determined with high accuracy, although the absolute values are somewhat uncertain and depend on the precision of the value of 23 V/nm for an LPE of 90 pJ. The field estimate for the first V + L run was calculated based on the CSR of Cr^{++}/Cr^+ at 50 pJ LPE compared to the CSRs from the laser run and subsequently by the relative voltage steps. The field estimates of the second V + L run were derived from the DR variation at the same LPE to the first V + L run, and the relative voltage changes. We refrain from showing absolute values as laser-mode evaporation of Fe_3O_4 showed a peculiar dependence of the CSR of Fe ions on the electrostatic field as well as LPE (Schreiber et al., 2014). In the case of chromia, we observe a consistent trend of CSRs for LPEs between 5 and 90 pJ, making our comparison feasible. Furthermore, we do not observe any significant amounts of O_2^+, suggesting higher fields as was the case in Schreiber et al. (2014). Figure 5 shows the O concentration as a function of the relative change in field. The plateau value of about 58 at% O is reached above a 40% increase compared to the initial field at 90 pJ LPE. The O concentrations measured for various DRs and temperatures fit well with the curve from the series of measurements done with varied LPE.

APT measurements of chromia and chromite with UV laser light with 355 nm wavelength (photon energy of 3.5 eV) have shown little influence of LPE on the O concentration (La Fontaine, et al., 2015*a*, 2015*b*). The O content measured in these studies was close to the expected value of 60 at% for the investigated LPEs between 22 and 115 pJ. It should be noted that the values of LPEs between different instruments cannot be compared, e.g., due to different spot sizes. The peak at 16 Da was ranged as O^+, and hence, a direct comparison is reasonable. We believe that the evaporation in this case happens through heating of the sample. Considering the reported bandgaps of chromia of 2.9 to 3.55 eV, the photon energy of 3.5 eV might be just below the threshold for strong

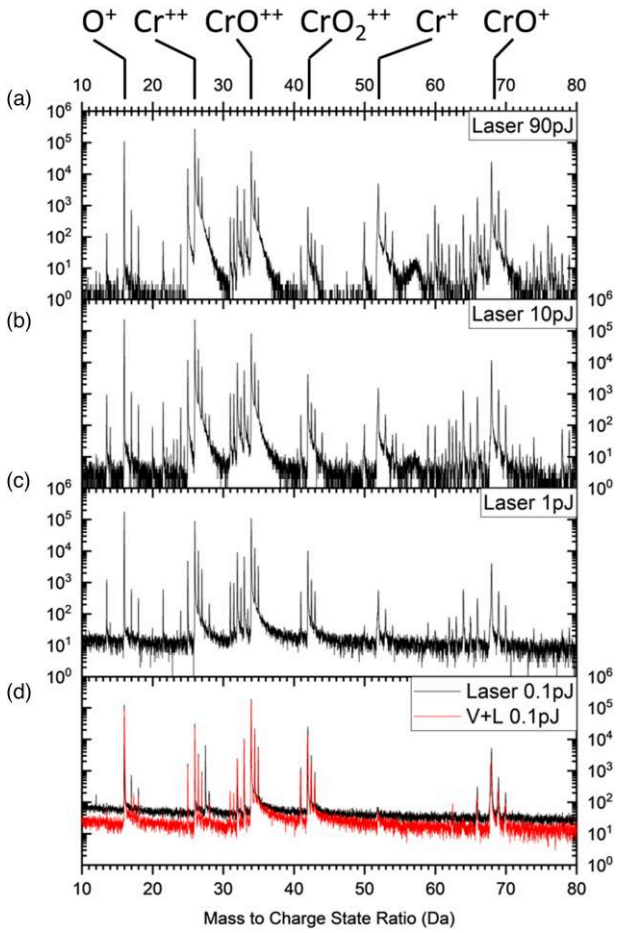

Fig. 2. Sections of mass spectra collected with different LPEs. The diagrams show number of counts as a function of mass to charge ratio. A direct comparison of laser and V + L runs at 0.1 pJ is shown in (d). The number of detected ions is about one million in each case.

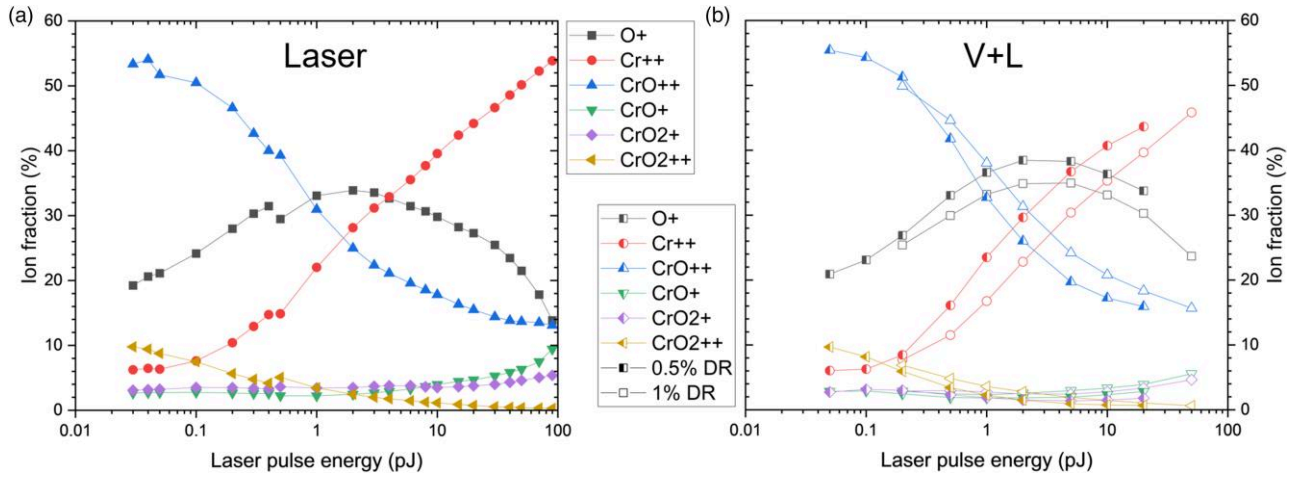

Fig. 3. Fractions of ions as a function of LPE in (a) laser and (**b**) V + L mode. Note that the half and open symbols correspond to different DRs during evaporation. In (a), the DR was set to 0.5%.

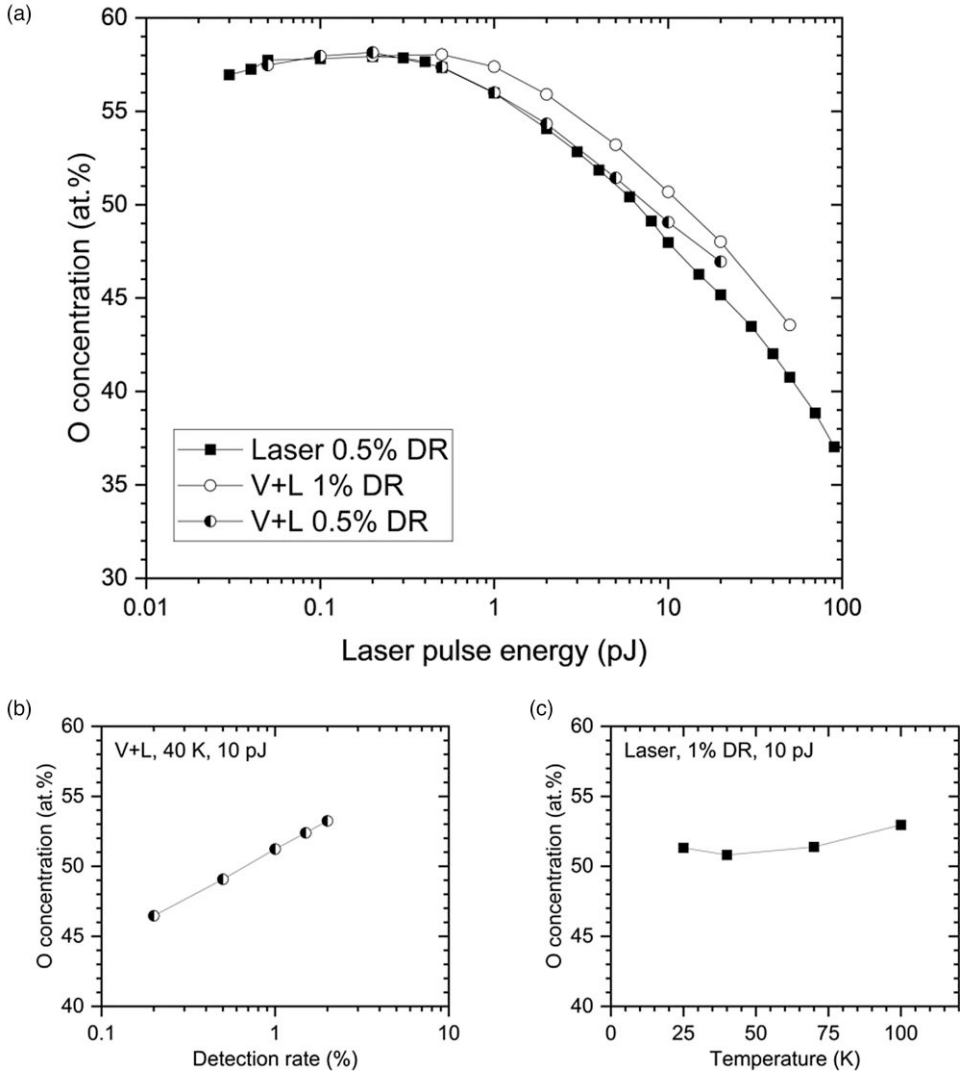

Fig. 4. Measured O concentration as a function of (a) LPE, (b) DR during V + L mode, and (c) temperature. Note that the *x*-axes in (a) and (b) are in logarithmic scale. Error bars from counting statistics are smaller than the symbol sizes and are not shown for visibility reasons.

Table 1. Peak Deconvolution Near 16 and 32 Da Performed in AP Suite.

Mass to charge ratio (Da)	16.0		16.5		17.0		17.5		18.0				
Ion	O^+	O_2^{++}	O_2^{++}	OH^+	O_2^{++}	O^+	O_2^{++}	OH_2^+	O^+	OH^+	O_2^{++}		
Natural abundance (%)	99.762	99.525	0.076	99.747	0.399	0.038	0.000	99.731	0.200	0.053	0.000		
Deconvoluted counts	175388	25417	0	525	101	66	6	0	344	0	0		
Mass to charge ratio (Da)	31.0	31.5	32.0		32.5		33.0		33.5			34.0	
Ion	TiO^{++}	TiO^{++}	O_2^+	TiO^{++}	TiO^{++}	CrO^{++}	TiO^{++}	O_2^+	TiO^{++}	CrO^{++}	CrO^{++}	O_2^+	TiO^{++}
Natural abundance (%)	8.229	7.422	99.525	73.564	5.439	4.335	5.322	0.076	0.013	0.002	83.599	0.399	0.010
Deconvoluted counts	1372	1245	854	12742	961	8040	1039	118	64	65	152777	0	0

The data set was measured at 1 pJ LPE during the laser run and contains 612,161 ions after background correction.

absorption (Henry et al., 2000; Guo et al., 2012). So, it is necessary to have a high LPE to provide the heating of the apex, and since little energy is provided to the sample, a high field is expected for the specimen leading to the observed good values of the measurement.

A similar dependence of the O content on LPE as in this work was observed for UV (355 nm wavelength) laser-assisted evaporation of MgO (Devaraj et al., 2013). The authors furthermore showed that the electrostatic field, shown by the CSR of Mg, is correlated with the LPE and the O content in a similar way as in this study. Field evaporation of SiO_2 and Al_2O_3 with extreme UV laser light (photon energy >> bandgap) shows good mass spectra and stoichiometry at low LPEs (Chiaramonti et al., 2020; Caplins et al., 2023). The introduced energy in these experiments is too low to heat the apex of the specimen significantly. The authors propose that

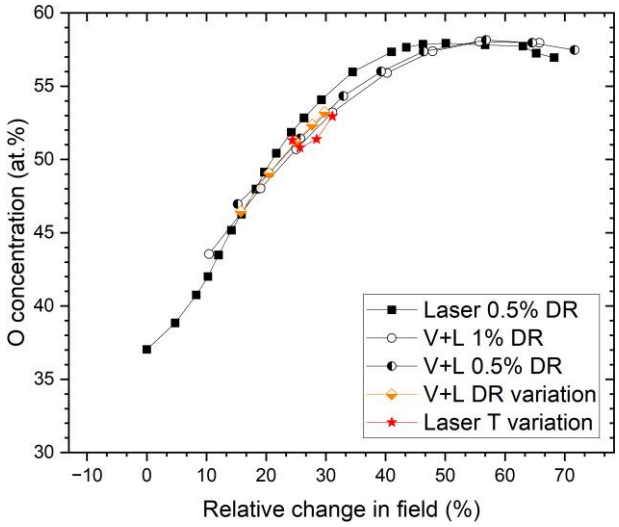

Fig. 5. O concentration as a function of the relative change in field at the apex of the specimens. See the text for the explanation of field estimates. Error bars derived from counting statistics are smaller than the symbol size and hence not shown for visibility reasons.

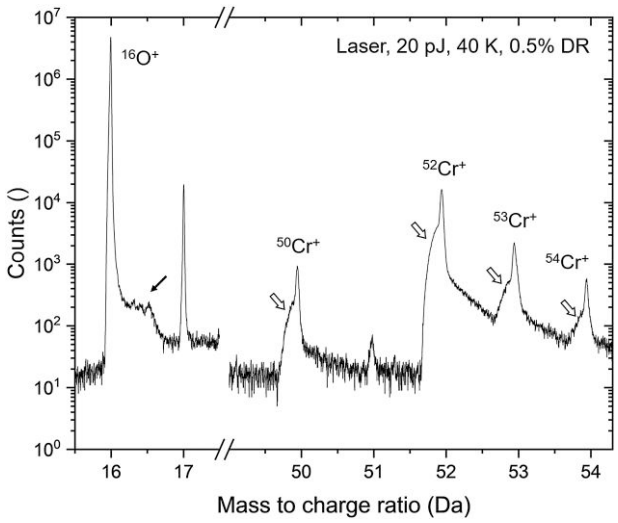

Fig. 6. Peak shape of O+ and Cr+ after detection of about 40 million ions at 20 pJ LPE. These ions were collected between LPE variations in the laser run.

a direct athermal photoionization with a thermal desorption might take place (Chiaramonti et al., 2020).

For photon energies higher than the bandgap, as for the 4.8 eV from the deep UV laser, absorption is high and the energy for localized heating or direct ionization is provided effectively. Hence, a low LPE can be used for evaporation of ions, whereas high LPEs lead to a lower electrostatic field necessary for constant evaporation. The deficiency in O when using high LPEs might come from the formation of neutral O atoms or O_2 molecules during dissociation of complex ions.

The bulk of the laser measurement, i.e., between the LPE variations, was done at 20 pJ, and the peak shapes are well pronounced to display certain anomalies. Figure 6 shows selected ranges of the mass spectrum of about 40 million collected ions. The peak at 16 Da shows a portion with increased counts at higher mass to charge ratios, whereas all the isotopes of Cr^+ display a shoulder toward lower mass to charge ratios. Additionally, CrO^+ shows an indication of a similar shoulder as Cr^+ (not shown in Fig. 6). One possible explanation for these peak shapes is the following: CrO^{++} could dissociate after initial acceleration toward the detector into Cr^+, which receives a higher kinetic energy than mono-atomic Cr^+ ions would get, and O^+, which receives a deficit in kinetic energy. The background-corrected additional counts at 16 Da correspond to only about 18% of the additional ions at the shoulders of Cr^+ and CrO^+. The measured O concentration at 20 pJ is 45 at% and still below the content expected from stoichiometry. Hence, other dissociation processes with neutral O are expected to happen. Double-charged peaks of Cr, CrO, and CrO_2 do not show anomalies in their peak shapes. This is reasonable since most dissociations would not lead to double-charged daughter ions. The full mass spectrum with ranges is shown in Supplementary Figure S5 in the supplementary material. Furthermore, the mass spectrum during ion collection at 0.5 pJ LPE is presented in Supplementary Figure S6 for comparison.

Judging from the comprehensive investigation of dissociation processes in Fe oxides of Kim et al. (2024), several dissociation processes might be similarly expected for chromia. The following dissociations resulting in neutral O were shown for Fe_2O_3:

$$FeO_4^+ \rightarrow FeO_2^+ + O_2$$

$$FeO_4^+ \rightarrow FeO^+ + O_3$$

$$FeO_4^{++} \rightarrow FeO_2^{++} + O_2$$

Furthermore, DFT calculations predicted the following dissociations with negative reaction energies (Kim et al., 2024):

$$FeO_2^+ \rightarrow Fe^+ + O_2$$

$$FeO_3^+ \rightarrow FeO^+ + O_2$$

The investigation into dissociation processes of molecular ions is limited in this study since the used APT instrument is equipped with a reflectron. This means that the trajectory of neutral atoms or molecules cannot reach the detector. A detailed analysis of dissociation lines of multiples, as shown by Saxey (2011), is therefore not meaningful.

For the investigation of chromia with deep UV laser-assisted field evaporation, we suggest a LPE of 0.5 to 1 pJ and 1 to 2% DR at common test temperatures, for the instrument used. This is considerably lower than LPE values used on other materials on this tool (Jakob & Thuvander, 2024; Mayweg et al., 2024) as well as on previous instruments with UV laser light. Applying higher LPEs than suggested above would result in an O deficiency between 10 and 25 at%. Using low LPEs can achieve more accurate O concentration measurements but leads to higher standing voltage and thus higher background signal as well as higher risk for fracture of the specimen. The V + L mode can achieve lower background at the same LPE and therefore widens the parameter window for the investigation of elements with low concentrations. Measurements were stable over the whole range of LPEs, and specimens fractured only below 0.2 pJ (at about 9 kV voltage).

Conclusion

Laser-assisted field evaporation of thermally grown chromia (Cr_2O_3) on a Ni-based alloy was performed with deep UV laser light. Smooth evaporation is maintained over more than three orders of magnitude variation in LPE. High LPEs lead to heavier molecular ions and a higher fraction of Cr^+ than low LPEs. It is shown that the accuracy of O measurements depends on the strength of the electrostatic field and hence only indirectly on the LPE. This is supported by the change in composition during variation of DR. The test temperature has only minor influence on the measured concentration. The apparent O deficiency is attributed to dissociation processes that lead to neutral O in the case of high LPEs. The used APT instrument is equipped with a reflectron and hence cannot detect neutral species.

Availability of Data and Materials

Datasets are available upon reasonable request.

Supplementary Material

To view supplementary material for this article, please visit https://doi.org/10.1093/mam/ozae111.

Acknowledgments

The experiments were performed at Chalmers Materials Analysis Laboratory (CMAL). The authors gratefully acknowledge Dr. Anton Chyrkin, Department of Chemistry, Chalmers University of Technology, for providing the sample material.

Financial Support

The current study hasn't received any fund from any organizations or institutions.

Conflict of Interest

The authors declare that they have no competing interest.

References

Bachhav M, Danoix F, Hannoyer B, Bassat JM & Danoix R (2013). Investigation of O-18 enriched hematite (α-Fe2O3) by laser assisted atom probe tomography. *Int J Mass Spectrom* **335**, 57–60. https://doi.org/10.1016/j.ijms.2012.10.012

Blum I, Rigutti L, Ois Vurpillot F, Vella A, Gaillard A & Deconihout B (2016). Dissociation dynamics of molecular ions in high dc electric field. *J Phys Chem A* **120**(20), 3654–3662. https://doi.org/10.1021/acs.jpca.6b01791

Caplins BW, Chiaramonti AN, Garcia JM, Sanford NA & Miaja-Avila L (2023). Atom probe tomography using an extreme ultraviolet trigger pulse. *Rev Sci Instrum* **94**(9), 093704. https://doi.org/10.1063/5.0160797

Chiaramonti AN, Miaja-Avila L, Caplins BW, Blanchard PT, DIercks DR, Gorman BP & Sanford NA (2020). Field ion emission in an atom probe microscope triggered by femtosecond-pulsed coherent extreme ultraviolet light. *Microsc Microanal* **26**(2), 258–266. https://doi.org/10.1017/S1431927620000203

Chyrkin A, Gunduz KO, Fedorova I, Sattari M, Visibile A, Halvarsson M, Froitzheim J & Stiller K (2022). High-temperature oxidation behavior of additively manufactured IN625: Effect of microstructure and grain size. *Corros Sci* **205**, 110382. https://doi.org/10.1016/j.corsci.2022.110382

Chyrkin A, Huczkowski P, Shemet V, Singheiser L & Quadakkers WJ (2011). Sub-scale depletion and enrichment processes during high temperature oxidation of the nickel base alloy 625 in the temperature range 900–1000°c. *Oxid Met* **75**(3–4), 143–166. https://doi.org/10.1007/s11085-010-9225-3

Danoix F, Grancher G, Bostel A & Blavette D (2007). Standard deviations of composition measurements in atom probe analyses-part II: 3D atom probe. *Ultramicroscopy* **107**(9), 739–743. https://doi.org/10.1016/j.ultramic.2007.02.005

Devaraj A, Colby R, Hess WP, Perea DE & Thevuthasan S (2013). Role of photoexcitation and field ionization in the measurement of accurate oxide stoichiometry by laser-assisted atom probe tomography. *J Phys Chem Lett* **4**(6), 993–998. https://doi.org/10.1021/jz400015h

Devaraj A, Perea DE, Liu J, Gordon LM, Prosa TJ, Parikh P, Diercks DR, Meher S, Kolli RP, Meng YS & Thevuthasan S (2018). Three-dimensional nanoscale characterisation of materials by atom probe tomography. *Int Mater Rev* **63**(2), 68–101. https://doi.org/10.1080/09506608.2016.1270728

Gault B, Moody MP, Cairney JM & Ringer SP (2012). *Atom Probe Microscopy*, vol. **160**. New York, NY: Springer.

Gault B, Saxey DW, Ashton MW, Sinnott SB, Chiaramonti AN, Moody MP & Schreiber DK (2016). Behavior of molecules and molecular ions near a field emitter. *New J Phys* **18**(3), 033031. https://doi.org/10.1088/1367-2630/18/3/033031

Gault B, Vurpillot F, Vella A, Gilbert M, Menand A, Blavette D & Deconihout B (2006). Design of a femtosecond laser assisted tomographic atom probe. *Rev Sci Instrum* **77**(4), 043705. https://doi.org/10.1063/1.2194089

Guo Y, Clark SJ & Robertson J (2012). Electronic and magnetic properties of Ti 2O 3, Cr 2O 3, and Fe 2O 3 calculated by the screened exchange hybrid density functional. *J Phys Condens Matter* **24**(32), 325504. https://doi.org/10.1088/0953-8984/24/32/325504

Haley D, London AJ & Moody MP (2020). Processing APT spectral backgrounds for improved quantification. *Microsc Microanal* **26**(5), 964–977. https://doi.org/10.1017/S1431927620024290

Henry S, Mougin J, Wouters Y, Petit JP & Galerie A (2000). Characterization of chromia scales grown on pure chromium in different oxidizing atmospheres. *Mater High Temp* **17**(2), 231–234. https://doi.org/10.1179/mht.2000.17.2.008

Hono K, Ohkubo T, Chen YM, Kodzuka M, Oh-ishi K, Sepehri-Amin H, Lia F, Kinno T, Tomiya S & Kanitani Y (2011). Broadening the applications of the atom probe technique by ultraviolet femtosecond laser. *Ultramicroscopy* **111**(6), 576–583. https://doi.org/10.1016/j.ultramic.2010.11.020

Jakob S & Thuvander M (2024). Revisiting compositional accuracy of carbides using a decreased detector efficiency in a LEAP 6000 XR atom probe instrument. *Microsc Microanal*, 1–9. https://doi.org/10.1093/mam/ozae069

Kim S-H, Bhatt S, Schreiber DK, Neugebauer J, Freysoldt C, Gault B & Katnagallu S (2024). Understanding atom probe's analytical performance for iron oxides using correlation histograms and ab initio calculations. *arXiv 12784*. https://doi.org/10.48550/arXiv.2401.12784, 23 January 2024, preprint: not peer reviewed.

Kingham DR (1982). The post-ionization of field evaporated ions: A theoretical explanation of multiple charge states. *Surf Sci* **116**(2), 273–301. https://doi.org/10.1016/0039-6028(82)90434-4

La Fontaine A, Gault B, Breen A, Stephenson L, Ceguerra AV, Yang L, Dinh Nguyen T, Zhang J, Young DJ & Cairney JM (2015*a*). Interpreting atom probe data from chromium oxide scales. *Ultramicroscopy* **159**, 354–359. https://doi.org/10.1016/j.ultramic.2015.02.005

La Fontaine A, Yen H-W, Felfer PJ, Ringer SP & Cairney JM (2015*b*). Atom probe study of chromium oxide spinels formed during intergranular corrosion. *Scr Mater* **99**, 1–4. https://doi.org/10.1016/j.scriptamat.2014.09.028

Langford RM & Rogers M (2008). In situ lift-out: Steps to improve yield and a comparison with other FIB TEM sample preparation techniques. *Micron* **39**(8), 1325–1330. https://doi.org/10.1016/j.micron.2008.02.006

Larson DJ, Prosa TJ, Ulfig RM, Geiser BP & Kelly TF (2013). *Local Electrode Atom Probe Tomography—A User's Guide*. New York: Springer.

London AJ (2019). Quantifying uncertainty from mass-peak overlaps in atom probe microscopy. *Microsc Microanal* **25**(2), 378–388. https://doi.org/10.1017/S1431927618016276

Lu X, Schreiber DK, Neeway JJ, Ryan JV & Du J (2017). Effects of optical dopants and laser wavelength on atom probe tomography analyses of borosilicate glasses. *J Am Ceram Soc* **100**(10), 4801–4815. https://doi.org/10.1111/jace.14987

Mancini L, Amirifar N, Shinde D, Blum I, Gilbert M, Vella A, Vurpillot F, Lefebvre W, Lardé R, Talbot E, Pareige P, Portier X, Ziani A, Davesnne C, Durand C, Eymery J, Butté R, Carlin JF, Grandjean N & Rigutti L (2014). Composition of wide bandgap semiconductor materials and nanostructures measured by atom probe tomography and its dependence on the surface electric field. *J Phys Chem C* **118**(41), 24136–24151. https://doi.org/10.1021/jp5071264

Mayweg D, Eriksson J, Sattari M, Sundell G, Limbäck M, Panas I, Andrén HO & Thuvander M (2024). Formation of pure zirconium islands inside c-component loops in high-burnup fuel cladding. *J Nucl Mater* **597**, 155116. https://doi.org/10.1016/j.jnucmat.2024.155116

Meisenkothen F, Steel EB, Prosa TJ, Henry KT & Prakash Kolli R (2015). Effects of detector dead-time on quantitative analyses involving boron and multi-hit detection events in atom probe tomography. *Ultramicroscopy* **159**(P1), 101–111. https://doi.org/10.1016/J.ULTRAMIC.2015.07.009

Miller MK & Forbes RG (2014). *Atom-Probe Tomography: The Local Electrode Atom Probe*. New York: Springer.

Morris RJH, Cuduvally R, Lin JR, Zhao M, Vandervorst W, Thuvander M & Fleischmann C (2022). Field dependent study on the impact of co-evaporated multihits and ion pile-up for the apparent stoichiometric quantification of GaN and AlN. *Ultramicroscopy* **241**, 113592. https://doi.org/10.1016/j.ultramic.2022.113592

Morris RJH, Lin J, Scheerder JE, Popovici MI, Meersschaut J, Goux L, Kar GS, van der Heide P & Fleischmann C (2024). Significant oxygen underestimation when quantifying barium-doped SrTiO layers by atom probe tomography. *Microsc Microanal* **30**, 49–58. https://doi.org/10.1093/micmic/ozad144

Nguyen TD, Zhang JQ & Young DJ (2015). Microstructures of chromia scales grown in CO2. *Mater High Temp* **32**(1–2), 16–21. https://doi.org/10.1179/0960340914Z.00000000056

Oberdorfer C, Stender P, Reinke C & Schmitz G (2007). Laser-assisted atom probe tomography of oxide materials. *Microsc Microanal* **13**(5), 342–346. https://doi.org/10.1017/S1431927607070274

Oltman E, Ulfig RM & Larson DJ (2009). Background removal methods applied to atom probe data. *Microsc Microanal* **15**(S2), 256–257. https://doi.org/10.1017/S1431927609095488

Peng Z, Vurpillot F, Choi PP, Li Y, Raabe D & Gault B (2018). On the detection of multiple events in atom probe tomography. *Ultramicroscopy* **189**, 54–60. https://doi.org/10.1016/j.ultramic.2018.03.018

Santhanagopalan D, Schreiber DK, Perea DE, Martens RL, Janssen Y, Khalifah P & Meng YS (2015). Effects of laser energy and wavelength on the analysis of LiFePO4 using laser assisted atom probe tomography. *Ultramicroscopy* **148**, 57–66. https://doi.org/10.1016/j.ultramic.2014.09.004

Saxey DW (2011). Correlated ion analysis and the interpretation of atom probe mass spectra. *Ultramicroscopy* **111**(6), 473–479. https://doi.org/10.1016/j.ultramic.2010.11.021

Schreiber DK, Chiaramonti AN, Gordon LM & Kruska K (2014). Applicability of post-ionization theory to laser-assisted field evaporation of magnetite. *Appl Phys Lett* **105**(24), 244106. https://doi.org/10.1063/1.4904802

Stiller K, Thuvander M, Povstugar I, Choi PP & Andrén HO (2016). Atom probe tomography of interfaces in ceramic films and oxide scales. *MRS Bull* **41**(1), 35–39. https://doi.org/10.1557/mrs.2015.307

Tang F, Gault B, Ringer SP & Cairney JM (2010). Optimization of pulsed laser atom probe (PLAP) for the analysis of nanocomposite Ti-Si-N films. *Ultramicroscopy* **110**(7), 836–843. https://doi.org/10.1016/j.ultramic.2010.03.003

Thompson K, Lawrence D, Larson DJ, Olson JD, Kelly TF & Gorman B (2007). In situ site-specific specimen preparation for atom probe tomography. *Ultramicroscopy* **107**(2–3), 131–139. https://doi.org/10.1016/j.ultramic.2006.06.008

Thuvander M, Shinde D, Rehan A, Ejnermark S & Stiller K (2019). Improving compositional accuracy in APT analysis of carbides using a decreased detection efficiency. *Microsc Microanal* **25**(2), 454–461. https://doi.org/10.1017/S1431927619000424

Thuvander M, Weidow J, Angseryd J, Falk LK, Liu F, Sonestedt M, Stiller K & Andrén HO (2011). Quantitative atom probe analysis of carbides. *Ultramicroscopy* **111**(6), 604–608. https://doi.org/10.1016/j.ultramic.2010.12.024

Ulfig R, Lenz D, Groth G, Bunton JH, Martin I, Prosa TJ, Reinhard DA, Clifton PH, Geiser BP & Larson DJ (2022). New product announcement—LEAP 6000XR, new applications, new performance. *Microsc Microanal* **28**(S1), 3190–3191. https://doi.org/10.1017/s1431927622011849

Viskari L, Hörnqvist M, Moore KL, Cao Y & Stiller K (2013). Intergranular crack tip oxidation in a Ni-base superalloy. *Acta Mater* **61**(10), 3630–3639. https://doi.org/10.1016/j.actamat.2013.02.050

Young DJ (2016). *High Temperature Oxidation and Corrosion of Metals*, 2nd ed. Amsterdam: Elsevier Ltd.